ADVANCED FUNCTIONAL MATERIALS

Supporting Information

for *Adv. Funct. Mater.,* DOI: 10.1002/adfm.201805184

Interplay between Structural and Thermoelectric Properties in Epitaxial $Sb_{2+x}Te_3$ Alloys

Stefano Cecchi, Daniele Dragoni, Dominik Kriegner, Elisa Tisbi, Eugenio Zallo, Fabrizio Arciprete, Václav Holý, Marco Bernasconi, and Raffaella Calarco*

Supporting Information

Interplay between Structural and Thermoelectric Properties in Epitaxial $Sb_{2+x}Te_3$ Alloys

Stefano Cecchi*, Daniele Dragoni, Dominik Kriegner, Elisa Tisbi, Eugenio Zallo, Fabrizio Arciprete, Vaclav Holy, Marco Bernasconi, Raffaella Calarco

1. X-ray Reflectivity

The XRR data of the $Sb_{2+x}Te_3$ samples on normal and miscut Si are plotted in Figure S1. The film thickness and the root-mean-square (rms) surface roughness have been obtained by fitting the reflectivity curves (these values are reported in Table S1). As shown by Cecchi et al., [1] the surface of epitaxial Sb_2Te_3 films on Si(111) is relatively rough, a consequence of the nucleation of Sb_2Te_3 domains which then coalesce forming a continuous film with smooth terraces and quintuple layer (QL) thick steps. Interestingly, the excess of Sb promotes a smoothening of the film surface which can be nicely followed by XRR. Pronounced thickness oscillations in the all measurement range can be seen for $Sb_{2+x}Te_3$ samples with $x > 1$ (see yellow and magenta curves). This effect may be directly related to the presence of Sb_{2n} blocks, which effectively diversifies the characteristic surface step structures, as reported for epitaxial $Bi_{2+x}Te_3$ films. [2] Also, considering that Sb is a well known surfactant, [3–6] it could alter the nucleation of $Sb_{2+x}Te_3$ from the very beginning. However, a conclusive understanding of this aspect requires dedicated experiments, which are not the focus of the present study. The roughness slightly increases for the samples with highest Sb content (blue curve), possibly related to a tradeoff between the beneficial excess of Sb and the growth conditions (namely fluxes ratio and growth rate). On miscut Si the surface roughness follows a trend similar to that observed for $Sb_{2+x}Te_3$ films on normal Si. The slight reduction of the

roughness with respect to the films grown on normal Si is promoted by the miscut substrate.

[7]

Table S1: Film thickness, growth rate and rms surface roughness of $Sb_{2+x}Te_3$ samples. Those grown on miscut Si are marked with an asterisk. The average alloy composition as calculated from the X-ray diffraction (XRD) fits is reported when available. Statistical errors for the estimated film thickness and rms roughness are below 0.3 nm.

Sample composition	Thickness [nm]	Growth rate [nm/min]	rms roughness [nm]
$Sb_{2.09}Te_3$	61.4	0.51	2.9
$Sb_{2.72}Te_3$	50.7	0.42	1.6
$Sb_{3.15}Te_3$	47.9	0.40	1.1
$Sb_{2+x}Te_3$	45.6	0.38	1.3
$Sb_{2+x}Te_3$	39.2	0.32	1.2
$Sb_{2.31}Te_3$*	25.1	0.28	2.6
$Sb_{3.3}Te_3$*	29.1	0.32	0.8
$Sb_{4.05}Te_3$*	33.5	0.37	0.9

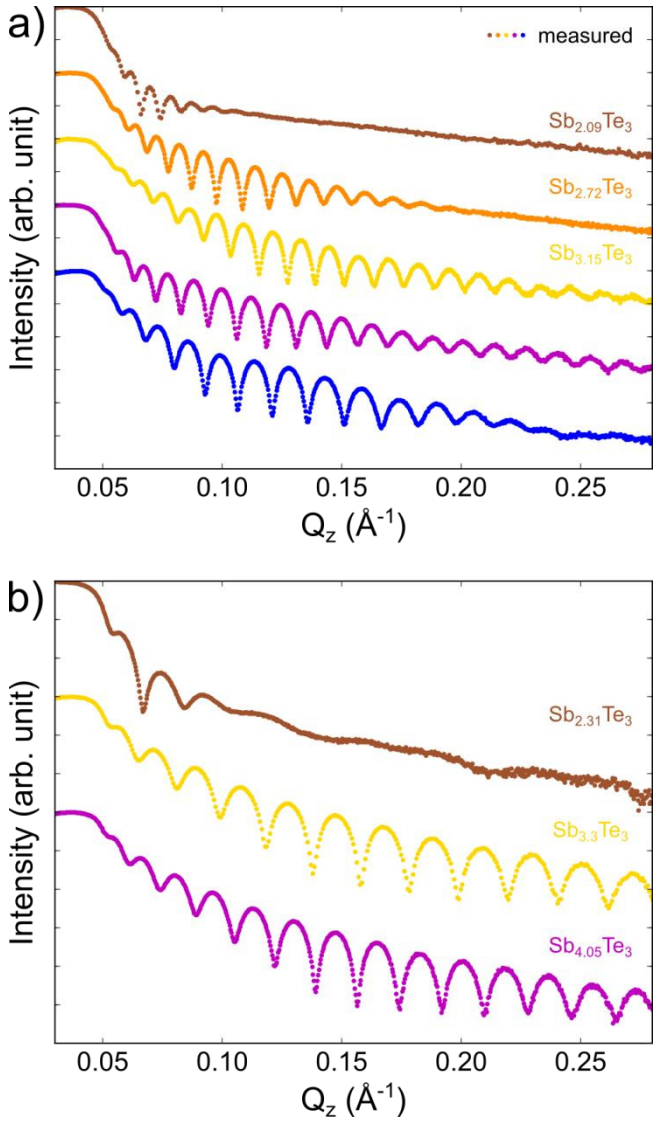

Figure S1: XRR measurements of $Sb_{2+x}Te_3$ samples grown on (a) normal Si(111) and (b) miscut Si(111). Sb_2Te_3 curves are plotted in brown, while orange, yellow, magenta and blue

curves correspond to Sb-rich samples with increasing excess of Sb. The curves are vertically shifted for clarity.

2. X-ray Diffraction Simulations

Our simulations of the diffraction signal of the $Sb_{2+x}Te_3$ thin films are based on the kinematical theory description of random chains of QL and Sb_2 or Sb_4 sequences. The diffraction intensity is thereby calculated in complete analogy to equations 15 and 16 in the work of Steiner et al.. [2] The description of the different building blocks thereby considers the following spacing of atomic planes: 1) d_1: distance of the Te-Te layers in a van der Waals (vdW) gap between two QLs; 2) d_2: distance of the Te-Sb layers adjacent to a vdW gap in a QL; 3) d_3: distance of the middle Sb-Te layers in a QL surrounded by other QLs; 4) d_4: distance of the second Sb-Te layers in a QL adjacent to the Sb-Sb double layer (DL); 5) d_5: distance of the Sb-Te layers in a QL adjacent to the Sb-Sb DL; 6) d_6: distance of the last Te layer in a QL from the first Sb layer in a DL; 7) d_7: distance between the layers in a Sb-Sb DL; 8) d_8: distance between two Sb-Sb DLs. Three scenarios visualizing the atomic spacing are given in Figure S2(a-c).

To describe our sample structure we assume that there is a number of QLs ≥ 1 between two Sb building blocks. The number of QLs is assumed to follow a Gamma distribution with parameters 'N_{QL}' and 'width'. The Sb building block can either be a Sb-Sb DL or with a propability of 'p_{Sb4}' also a stack of two such DLs, i.e. 4 Sb layers. Using the atomic plane distance d_1 to d_8, the statistical parameters described in this paragraph, as well as scaling parameters for primary beam intensity and background we fit the model curves to our experimental data.

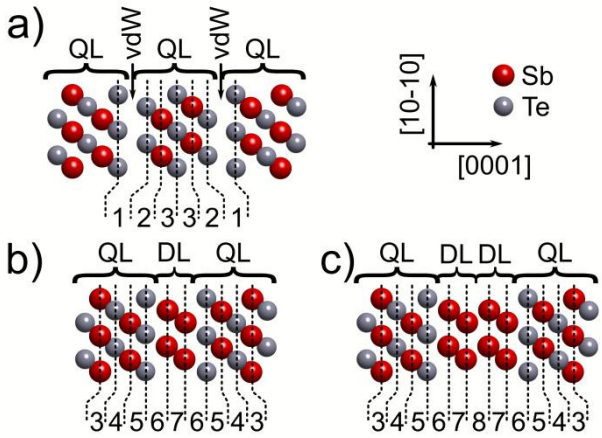

Figure S2: Sketch of the atomic structure of building blocks of $Sb_{2+x}Te_3$. Panel (a) shows the atomic arrangement in a stack of multiple quintuple layers (QLs) as they appear in the Sb_2Te_3 phase. (b) and (c) show the inclusion of Sb-Sb double layers (DLs) between QLs. In all panels the numbers of 1-8 correspond to the atomic spacings d_{1-8} used in the simulations.

The relevant parameters from the fits are collected in Table S2.

Table S2: Relevant parameters fitted for $Sb_{2+x}Te_3$ samples on normal and miscut Si. Those grown on miscut Si are marked with an asterisk. Statistical errors for N_{QL}, width and p_{Sb4}, obtained from the least squares optimization, are below 5% of the respective value.

Sample composition	N_{QL} [# QLs]	width [# QLs]	N_{QL}/width [1]	p_{Sb4} [%]
$Sb_{2.09}Te_3$	24.7	12.2	2.0	21
$Sb_{2.72}Te_3$	3.5	2.2	1.6	25
$Sb_{3.15}Te_3$	2.0	1.8	1.1	18
$Sb_{2.31}Te_3$*	9.4	5.1	1.8	77
$Sb_{3.3}Te_3$*	1.7	1.0	1.7	22
$Sb_{4.05}Te_3$*	1.0	0.5	2.0	14

3. Energy dispersive X-ray spectroscopy

Energy dispersive X-ray spectroscopy (EDX) measurements were performed for the $Sb_{2+x}Te_3$ samples grown on miscut Si(111). These were performed in a scanning electron microscope using 6, 8, and 10 keV beam energy of the electrons. The recorded emission spectra contain the K-line of the Si substrate and the L lines of Sb and Te (not shown). The quantification of the composition of the thin films was performed using the STRATAGem software from SAMx. [8] Combining the spectroscopic data of the three excitation energies and using the known energy dependence of fluorescence intensities an error between 1 and 2 at.% is achieved. In Table S3 the film composition values measured by EDX are compared with those

calculated from the XRD fits. There is a general good agreement between EDX and XRD composition values, the last ones being at the upper part of the given EDX compositional range.

Table S3: Film composition values measured by EDX of the $Sb_{2+x}Te_3$ samples grown on miscut Si(111). The compositional range is calculated with an error of 1 at.%.

Sample composition (XRD)	Sample composition (EDX with ±1 at.%)
$Sb_{2.31}Te_3$	$Sb_{2.16\text{-}2.35}Te_3$
$Sb_{3.3}Te_3$	$Sb_{3.07\text{-}3.3}Te_3$
$Sb_{4.05}Te_3$	$Sb_{3.56\text{-}3.86}Te_3$

4. Raman Spectroscopy

The Raman spectroscopy data of the $Sb_{2+x}Te_3$ samples grown on miscut Si(111) are shown in Figure S3(a). We found qualitatively no difference between these spectra and those of $Sb_{2+x}Te_3$ alloys on normal Si (Figure 3(a)). The spectrum of $Sb_{2.31}Te_3$ is very similar to that of $Sb_{2.09}Te_3$, although the slight excess of Sb in the film. The Raman shift of the $A_{1g}^{(1)}$ and $E_g^{(2)}$ modes as a function of the excess of Sb in the films is plotted in Figure S3(b), black and gray respectively. The red shift for the $A_{1g}^{(2)}$ mode (not shown) is within 1%, again highlighting the weaker link between this mode and the film composition.

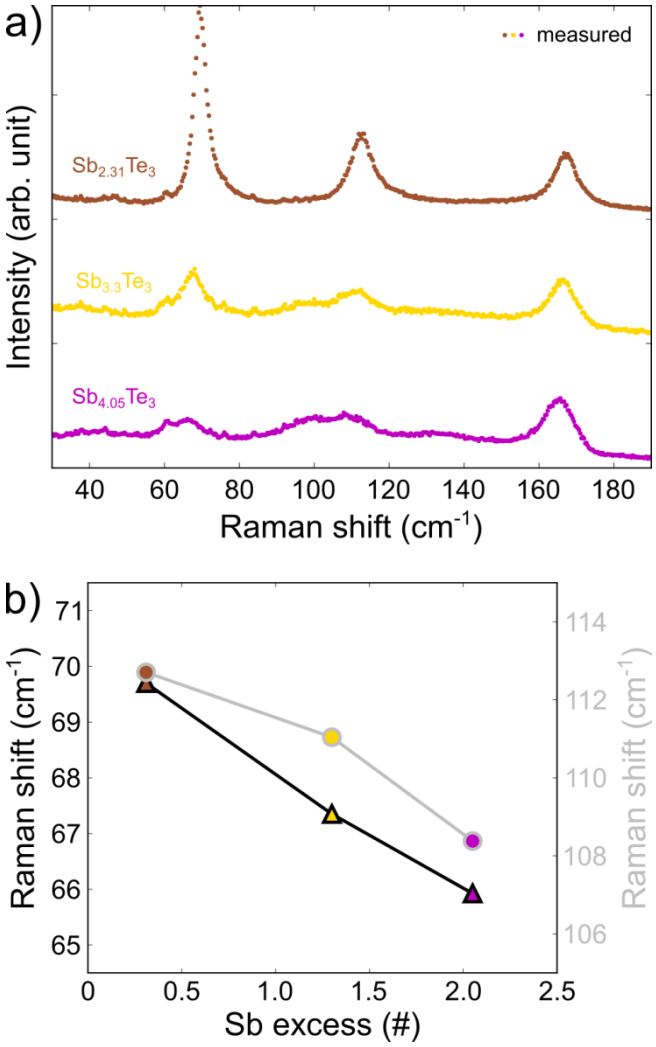

Figure S3: (a) Raman spectra of $Sb_{2+x}Te_3$ samples grown on miscut Si(111). $Sb_{2.31}Te_3$, $Sb_{3.3}Te_3$ and $Sb_{4.05}Te_3$ curves are plotted in brown, yellow and magenta respectively. The curves are vertically shifted for clarity. (b) Raman shift of the $A_{1g}^{(1)}$ (black) and $E_g^{(2)}$ (gray) modes as a function of the excess of Sb in the films.

The Raman spectrum of the $Sb_{2.09}Te_3$ sample shown in Figure 3(a) is compared with those of a reference Sb_2Te_3 [9] and a Sb_2Te_3 sample with strong excess of Te (see Figure S4). The formation of Te segregated in the samples is at the origin of the peaks at 92, 119 and 140 cm^{-1}.

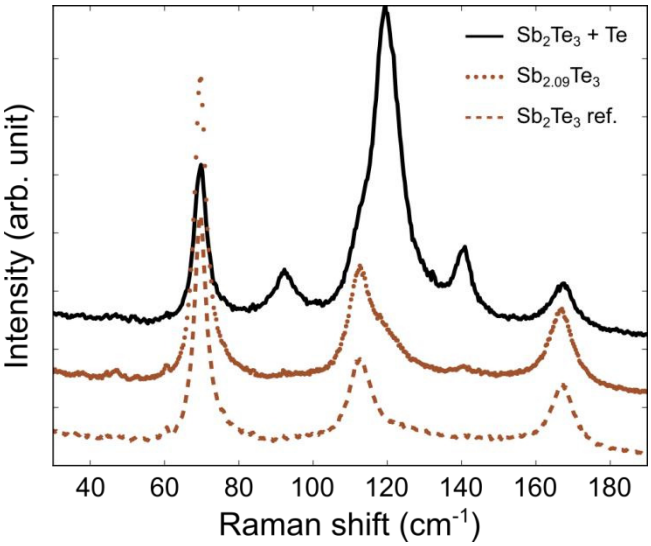

Figure S4: Raman spectra of $Sb_{2.09}Te_3$ (dotted brown), a reference Sb_2Te_3 (dashed brown) and a Sb_2Te_3 with Te segregated (solid black). All the samples are grown on normal Si(111). The curves are vertically shifted for clarity.

5. Density Functional Theory Calculations

The optimized lattice parameters of the two possible structures of Sb_4Te_3 (1/1 and 2/2), calculated within density functional theory (DFT), are reported in Table S4.

Table S4: Theoretical equilibrium lattice parameters (hexagonal notation). The experimental data of Ref. [10,11] are also reported.

Structure	Functional	a(Å)	c(Å)
1/1	PBE+D2	4.260	41.012
2/2	PBE+D2	4.252	82.591
2/2	Exp.	4.271(1)	83.564(2)

6.Density Functional Perturbation Theory Calculations

The phonon frequencies at the Γ point are calculated for the two relaxed structures within density functional perturbation theory (DFPT). Since the system is actually slightly metallic we did not include the non-analytical contribution to the dynamical matrix giving rise to LO-TO splittings. We computed the Raman cross section by finite differences (0.01 Å) of the susceptibility tensor with respect to the atomic displacement according to Equations 7 and 8 in Ref. [12] to which we refer for all details.

We considered back-scattering geometry with non-polarized light. The same scheme was used for the calculation of the Raman spectrum of Sb_2Te_3 in Ref. [12] (also shown in Figure 3(b)). The theoretical spectrum Sb_2Te_3 is in a good agreement with experiments in the position of the peaks, but the intensity of the peak at 117 cm^{-1} (E_g mode) is largely overestimated in the theoretical spectrum. Such discrepancy can be attributed to the non-resonant condition which is assumed in our theoretical approach as opposed to the resonant condition that actually occurs in experiments. The peaks at 67 and 169 cm^{-1} in Sb_2Te_3 are due to A_{1g} modes.

6.1. Sb_4Te_3

The phonon frequencies at the Γ point, calculated for the two relaxed structures within DFPT, are reported in Table S5.

Table S5: Calculated optical phonon frequencies (cm^{-1}) at the Γ point for the 1/1 and 2/2 structures. All u modes are IR active and all g modes are Raman active. The substructures of the crystal (Sb or Sb_2Te_3 layers) over which phonons are mostly localized are given in the last column (Loc.). The modes with mixed character involve equally the Sb and Sb_2Te_3 layers.

1/1		2/2	
ω (cm^{-1})	Loc.	ω (cm^{-1})	Loc.
31 - E_u	+Sb, −Sb_2Te_3	17 - E_g	Sb_2Te_3
38 - A_{2u}	+Sb, −Sb_2Te_3	23 - E_u	Sb
46 - E_g	Sb_2Te_3	24 - A_{1g}	Sb_2Te_3
62 - A_{1g}	Sb_2Te_3	27 - A_{2u}	+Sb, −Sb_2Te_3
92 - E_u	Sb_2Te_3	44 - E_g	mixed
102 - E_u	Sb_2Te_3	45 - E_u	Sb_2Te_3
110 - A_{2u}	Sb_2Te_3	49 - E_g	mixed
110 - E_g	Sb_2Te_3	54 - A_{1g}	+Sb, −Sb_2Te_3
146 - E_g	Sb_2Te_3	61 - A_{2u}	Sb_2Te_3
146 - E_g	Sb	67 - A_{1g}	−Sb, +Sb_2Te_3
160 - A_{1g}	−Sb, +Sb_2Te_3	86 - E_u	Sb_2Te_3
171 - A_{1g}	Sb	97 - E_g	Sb_2Te_3
-		99 - E_u	Sb_2Te_3
-		103 - E_g	Sb_2Te_3
-		112 - A_{2u}	Sb_2Te_3
-		114 - E_g	Sb_2Te_3
-		114 - E_u	Sb_2Te_3
-		115 - A_{1g}	Sb_2Te_3
-		138 - E_g	Sb
-		149 - A_{2u}	Sb_2Te_3
-		150 - E_u	Sb
-		159 - A_{1g}	+Sb, −Sb_2Te_3
-		166 - A_{1g}	mixed, −Sb, +Sb_2Te_3
-		166 - A_{2u}	−Sb, +Sb_2Te_3
-		169 - A_{1g}	mixed
-		170 - A_{2u}	Sb

In the theoretical spectra of Sb_4Te_3 we can identify five main features as detailed below. i) The peaks at 62 cm^{-1} (1/1) and 67 cm^{-1} (2/2) which are due to an A_{1g} mode involving mostly the Sb_2Te_3 layers correspond to the theoretical mode at 67 cm^{-1} of the Sb_2Te_3 crystal. [12] The displacement patterns of these modes, highlighted in Figure 3(b) with full brown squares, are shown in Figure 3(c and d). ii) The peak at about 110 cm^{-1} (1/1) and 114 cm^{-1} (2/2) is an E_g mode involving mostly the motion of the Sb_2Te_3 layers which directly relates to the theoretical mode at 117 cm^{-1} of the Sb_2Te_3 crystal. [12] iii) The peak at about 97 cm^{-1} (2/2) is also an E_g mode localized on Sb_2Te_3 with the two Sb_2Te_3 layers in anti-phase, opposite to the E_g mode at 114 cm^{-1} where the two Sb_2Te_3 layers oscillate in phase. This mode can be seen as a mixture of the $E_u^{(2)}$ and $E_u^{(3)}$ at the zone boundary along c of the Sb_2Te_3 crystal (see Figures 3 and 4 in Ref. [12]). No corresponding mode is found for Sb_4Te_3 (1/1) and Sb_2Te, both having a single Sb_2Te_3 QLs in between Sb slabs. Therefore, this mode is a signature of adjacent Sb_2Te_3 QLs characteristic of the Sb_4Te_3 2/2 structure. iv) The peak at 146 cm^{-1} in the 1/1 structure is due to an E_g mode involving only the motion of the Sb bilayers (see Figure 3(e and f)) which correlates with the E_g mode of the single self-standing bilayer at 150 cm^{-1}. This peak shifts to 138 cm^{-1} in the 2/2 structure which displays two bilayers. This peak, highlighted in Figure 3(b) with full red circles, consistently moves closer to the Sb bulk-like value of 115 cm^{-1} for the E_g mode when increasing the number of Sb bilayers. v) In Sb_4Te_3 we observe a splitting of the peak at 169 cm^{-1} of Sb_2Te_3 into a doublet at 160-171 cm^{-1} (1/1) and 159-166 cm^{-1} (2/2) due to two A_{1g} modes. The peak at 171 cm^{-1} (1/1) is an A_{1g} mode involving the motion of the Sb bilayer which corresponds to the mode at 185 cm^{-1} of the self-standing Sb bilayer. This mode evolves into that at 159 cm^{-1} in the 2/2 structure, moving closer to the A_{1g} mode of bulk Sb at 150 cm^{-1}. This mode is highlighted in Figure 3(b) with empty red circles. The modes at 160 cm^{-1} (1/1) and 166 cm^{-1} (2/2), highlighted in Figure 3(b) with empty brown squares, involve mostly the motion of the Sb_2Te_3 layers with a partial mixing with the motion of the Sb layers (see Figure 3 (g-j)). These correspond to the 169 cm^{-1} mode of pure Sb_2Te_3

which consistently shifts to higher frequency by increasing the number of QLs in between Sb_{2n} slabs.

6.2. Sb_2Te

The crystal structure of Sb_2Te belongs to the P-3m1 space group as suggested by Agafonov. [13] It can be described by a stacking of two Sb_2 layers and a single Sb_2Te_3 layer along the c axis of the standard hexagonal cell. The cell contains 9 atoms whose positions are given in Ref. [13] along with the cell parameters.

We have performed on this structure DFT and DFPT calculations as those described for Sb_4Te_3. The initial structure with atomic positions was taken from Ref. [13] and then fully relaxed. The optimized lattice parameters, calculated within DFT, are reported in Table S6.

Table S6: Theoretical equilibrium lattice parameters for Sb_2Te (hexagonal cell) obtained by DFT-PBE calculations or by adding vdW corrections (PBE+D2). Experimental data from Ref. [13] are also reported.

Functional	a(Å)	c(Å)
PBE	4.348	17.628
PBE+D2	4.266	17.273
Exp.	4.272(1)	17.633(3)

The phonon frequencies at the Γ point are calculated for the relaxed structure within DFPT. The results are reported in Table S7.

Table S7: Calculated optical phonon frequencies (cm^{-1}) at the Γ point for Sb_2Te with PBE+D2 functional. All u modes are IR active and all g modes are Raman active. The substructures of the crystal (Sb or Sb_2Te_3 layers) over which phonons are mostly localized are given in the last column (Loc.). Some modes with mixed character involve equally the Sb and Sb_2Te_3 layers.

	PBE+D2
ω (cm^{-1})	Loc.
28 - E_u	+Sb,−Sb_2Te_3
34 - A_{2u}	+Sb,−Sb_2Te_3 mixed
42 - E_g	mixed
52 - A_{1g}	+Sb, −Sb_2Te_3
53 - E_g	mixed
67 - A_{1g}	Sb_2Te_3
96 - E_u	Sb_2Te_3
103 - E_u	Sb_2Te_3
106 - E_g	Sb_2Te_3
112 - A_{2u}	Sb_2Te_3
135 - E_g	Sb
144 - A_{2u}	Sb_2Te_3
149 - E_u	Sb
155 - A_{1g}	mixed
165 - A_{1g}	mixed
169 - A_{2u}	Sb

7. Electrical Characterization

The linear relationship between the hole concentration and the excess of Sb in the $Sb_{2+x}Te_3$ alloys is shown in Figure S5. Please note that the linear fit (dashed black) is meant as guide to the eyes, while a more accurate fit would require measurements of a stoichiometric Sb_2Te_3 sample.

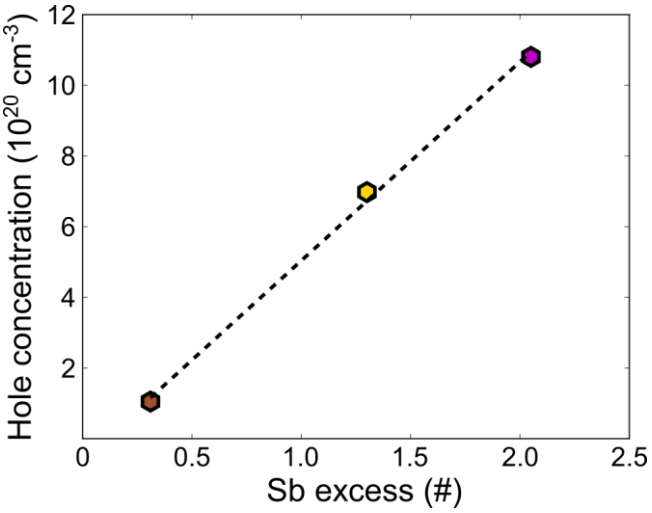

Figure S5: Room temperature hole concentration (hexagons) as a function of the Sb excess, calculated from the XRD fits, of the $Sb_{2+x}Te_3$ films grown on miscut Si. The linear fit (dashed black) is a guide to the eyes.

The electrical conductivity σ and the power factor $S^2\sigma$ as a function of the Sb excess are shown in Figure S6, circles and diamonds respectively.

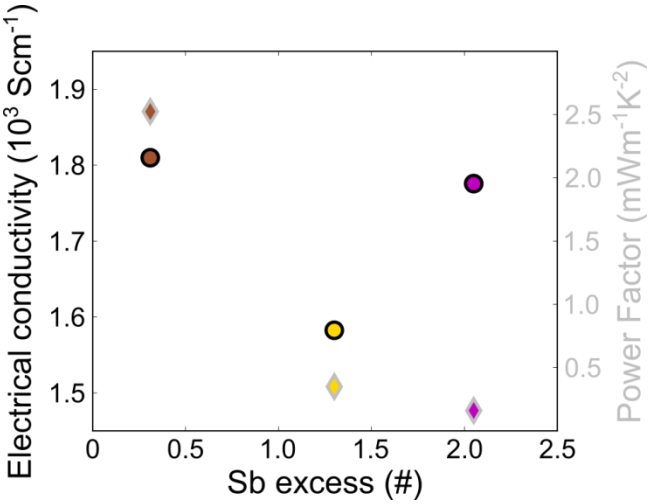

Figure S6: Room temperature electrical conductivity (circles with black borders) and power factor (diamonds with gray borders) as a function of the Sb excess of the $Sb_{2+x}Te_3$ films grown on miscut Si.

References

[1] S. Cecchi, R. N. Wang, E. Zallo, R. Calarco, Nanosci. Nanotechnol. Lett. **2017**, 9, 1114.

[2] H. Steiner, V. Volobuev, O. Caha, G. Bauer, G. Springholz, V. Holý, J. Appl. Crystallogr. **2014**, 47, 1889.

[3] K. Sakamoto, K. Miki, T. Sakamoto, H. Yamaguchi, H. Oyanagi, H. Matsuhata, K. Kyoya, Thin Solid Films **1992**, 222, 112.

[4] C. W. Pei, B. Turk, J. B. Héroux, W. I. Wang, J. Héroux, *J. Vac. Sci. …* **2001**, 19, 1426.

[5] T. Kageyama, T. Miyamoto, M. Ohta, T. Matsuura, Y. Matsui, T. Furuhata, F. Koyama, J. Appl. Phys. **2004**, 96, 44.

[6] E. A. Anyebe, M. K. Rajpalke, T. D. Veal, C. J. Jin, Z. M. Wang, Q. D. Zhuang, Nano Res. **2015**, 8, 1309.

[7] E. Zallo, S. Cecchi, J. E. Boschker, A. M. Mio, F. Arciprete, S. Privitera, R. Calarco, Sci. Rep. **2017**, 7, 1466.

[8] Http://www.samx.com/microanalysis/products/stratagem_us.html, STRATAGem.

[9] S. Cecchi, E. Zallo, J. Momand, R. Wang, B. J. Kooi, M. A. Verheijen, R. Calarco, APL Mater. **2017**, 5, 026107.

[10] P. F. P. Poudeu, M. G. Kanatzidis, Chem. Commun. **2005**, 2672.

[11] Sb4Te3 Crystal Structure: Datasheet from “PAULING FILE Multinaries Edition – 2012” in SpringerMaterials (https://materials.springer.com/isp/crystallographic/docs/sd_1420181).

[12] G. C. Sosso, S. Caravati, M. Bernasconi, J. Phys. Condens. Matter **2009**, 21, 095410.

[13] V. Agafonov, N. Rodier, R. Céolin, R. Bellissent, C. Bergman, J. P. Gaspard, Acta Crystallogr. Sect. C Cryst. Struct. Commun. **1991**, 47, 1141.